Optimization of Drift Chamber Performance for The Q_{weak} Experiment

A thesis submitted in partial fulfillment of the requirement for the degree of Bachelor of Science with Honors in Physics from the College of William and Mary in Virginia,

by

Peyton W. Rose

Advisor: Prof. David Armstrong

Prof. Charles Perdrisat

Prof. Todd Averett

Prof. Sarah Day

Williamsburg, VA
May 2011

Abstract

The Q_{weak} experiment, currently running at Jefferson Lab, uses parity-violating electron-proton scattering to measure the weak charge of the proton. The weak charge of the proton, Q_w^p, is explicity predicted by the Standard Model of particle physics. Thus, by comparing Q_{weak}'s experimentally determined value to the theoretically predicted value of Q_w^p, this experiment will test the standard model. One component of the experimental apparatus is a set of four vertical drift chambers, constructed at the College of William and Mary. These drift chambers are used to track electrons in the Q_{weak} experiment. The research presented in this paper focuses on optimizing the performance of these drift chambers, by analyzing how their behavior varies with operating conditions. Optimizing the performance of these chambers will help Q_{weak} to keep experimental uncertainties to a minimum.

Contents

List of Figures

List of Tables

Chapter 1

Introduction

The Standard Model of particle physics is a theory, developed in the 1970s, which describes the fundamental particles of nature and the electromagnetic, strong, and weak interactions that act on these particles. To date, the Standard Model has been extremely successful in predicting experimental outcomes, but it is known to be an incomplete theory. Among other issues, it does not account for the gravitational force, and it requires that over twenty of its parameters be determined from experiment. Because it is incomplete, physicists conduct experiments to search for evidence of physics beyond the Standard Model.

This search for new physics is conducted in two ways. High-energy experiments accelerate existing particles to ultra-relativistic speeds and collide them into each other in an attempt to generate previously unobserved forms of matter. Any newly detected particles would need a place in future extensions of the Standard Model. At the other end of the energy spectrum, low-energy experiments make precise measurements of values predicted by the Standard Model. Disparities between the theoretically predicted values and their corresponding experimental measurements would provide evidence

for physics beyond the Standard Model. Any future extensions of this theory would be constrained by these precision measurements. The Q_{weak} Experiment is one of these low-energy, high precision experiments, currently running at Jefferson Lab, Newport News, VA. This experiment will test the Standard Model by making a precision measurement of the proton's weak charge through parity-violating electron scattering.

The purpose of the research presented in this paper was to evaluate and optimize the performance of Q_{weak}'s vertical drift chambers. These drift chambers consist of two wire planes contained in a gas mixture, and are used to track electrons in the Q_{weak} apparatus. As elastically scattered electrons pass through these drift chambers, their position and direction are determined. The efficiency with which scattered electrons can be detected, and the accuracy with which their tracks can be reconstructed depend on several operating conditions. Performance results from past tracking runs are presented, and the data will be used to optimize running conditions for future tracking runs.

Chapter 2

The Q_{weak} Experiment

2.1 Overview

The Q_{weak} Experiment will use parity-violating electron-proton $(e-p)$ scattering to measure the weak charge of the proton, Q_w^p. In the experiment, a polarized beam of electrons elastically scatters off of a liquid hydrogen target. These electrons are then detected, and the results will allow for a calculation of Q_w^p. The goal is to test the Standard Model of particle physics by making a precise measurement of Q_w^p, and comparing the theoretically predicted value to the experimentally determined value. The measurement will be made at low four-momentum transfer (Q^2) in order to minimize contributions from the proton's internal structure. The combined systematic and statistical error in the measurement of Q_w^p will be 4%.

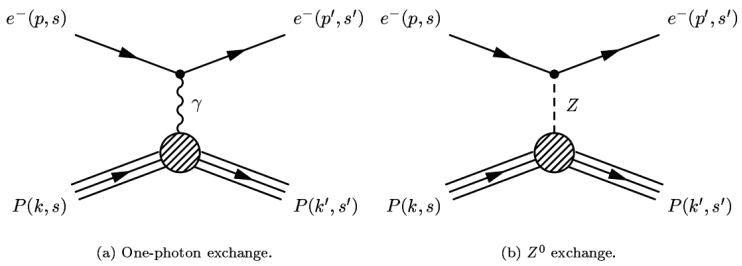

(a) One-photon exchange. (b) Z^0 exchange.

Figure 2.1: $e-p$ Scattering: These Feynman diagrams show the fundamental interactions involved in the Q_{weak} experiment. Electrons scatter off the liquid hydrogen target via the electromagnetic and weak forces. Image from [1].

2.2 The Weak Interaction

There are two types of weak interactions, and they both act on all leptons and quarks [2]. Charged weak interactions are mediated by the $W^{\pm}$ bosons, while the Z^0 boson mediates neutral weak interactions. As the names imply, neutral weak interactions leave the charges of the interacting leptons and quarks fixed, while charged weak interactions alter the charge (and therefore identity) of the interacting particles. Since charged weak interactions change the identity of the interacting particles, this interaction is responsible for some classes of particle decay in nature. One unique feature of weak interactions is that the $W^{\pm}$ and Z^0 bosons do not act equivalently on all particles. A W^+ boson acts only on a fermion whose spin is parallel to its velocity (right-handed); a W^- boson acts only on a fermion whose spin is anti-parallel to its velocity (left-handed); the Z^0 boson acts on both types of fermions, but with differing magnitudes for the different handedness. Q_{weak} uses this unique feature of the weak interaction to measure Q_w^p. To further understand why this effect is significant, we must consider the parity

operator, discussed next.

2.3 Parity

In a physical process, the parity operator changes the sign of all spatial coordinates [3]. More specifically, it will convert a right-handed coordinate system into one that is left-handed. For example, in a three-dimensional Cartesian coordinate system defined by unit vectors $\hat{x}$, $\hat{y}$, and $\hat{z}$, a parity operation would convert these unit vectors into -$\hat{x}$, -$\hat{y}$, and -$\hat{z}$. A parity operation is shown in Figure 2.2.

Performing this operation on a system is equivalent to observing a mirror image of the physical process being studied. Originally, physicists believed that the laws of nature were invariant under such a transformation. Experimental evidence supported this assumption for the electromagnetic and strong interactions. However, in 1956, Lee and Yang [4] suggested that parity-violation might occur in weak interactions. This suggestion was confirmed in an experiment by Wu [5], who observed the direction of emitted electrons during the beta decay of Cobalt 60. It was found that most electrons were emitted in the direction opposite to the nuclear spin. In a mirror image of this process, electrons would be emitted in the direction of the nuclear spin. However, this mirror process does not occur in nature and therefore, the interaction does not conserve parity.

In the Q_{weak} experiment, polarized electrons are focused onto a liquid hydrogen target. Suppose a right-handed electron in this experiment has momentum, $\vec{p_0}$ and spin, $\vec{s_0}$, given by $\vec{s_0} = \vec{r_0}$ x $\vec{p_0}$. The spin projected onto

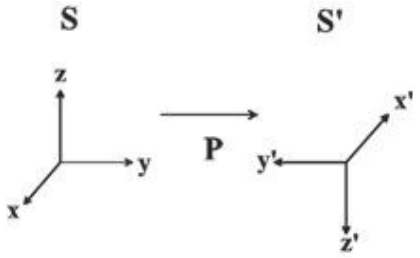

Figure 2.2: Parity Operation: This Figure shows a parity transformation, P, acting a a right-handed coordinate system, S. P transforms S into a left-handed coordinate system, S'.

the direction of momentum is then given by $T_0 = s_0 * p_0$. Performing a parity operation on these quantities gives $\vec{r'} = -\vec{r_0}$ and $\vec{p'} = -\vec{p_0}$. Then, $\vec{s'} = -\vec{r_0}$ x -$\vec{p_0} = \vec{s_0}$. Projecting the spin onto the direction of momentum gives $T' = \vec{s'} * \vec{p'} = \vec{s_0} * -\vec{p_0} = -T_0$. More simply, we find that performing a parity operation on our right-handed electron, transforms it into a left-handed electron. This is significant because (as discussed above) the neutral weak interaction acts with different magnitudes on these different electrons. Thus, the Q_{weak} Experiment will see an asymmetry in scattering for right- and left-handed electrons, and this asymmetry will be used to extract the proton's weak charge from experimental data.

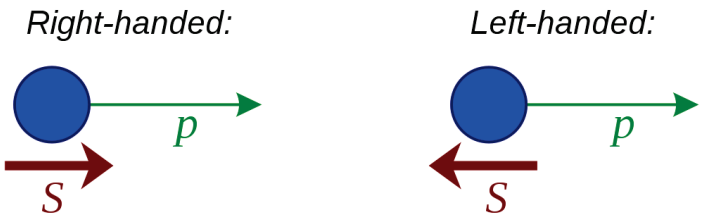

Figure 2.3: Particle Handedness: Here we see both a right- and left-handed particle. Right-handed particles have their spin aligned with their momentum. For left-handed particles, their spin and momentum are anti-parallel. The parity operator transforms a right-handed particle into one that is left-handed.

2.4 Physics of Q_{weak}

Physicists use the term weak charge to describe how particles 'feel' the weak interaction. In the Standard Model, the weak charge of the proton is predicted [6] as

$$Q_w^p = 1 - 4\sin^2(\theta_w). \tag{2.1}$$

Here, θ_w is the weak mixing angle, which is a function of the energy at which it is probed. This relationship between $\sin^2(\theta_w)$ and energy is shown in Figure 2.4 [6]. The blue lines gives the Standard Model prediction, while the black points correspond to experimental results (with error bars). The red points indicate future experiments, and are placed arbitrarily on the graph. The size of the error bars for these future measurements gives the anticipated uncertainty in the measurement.

To reduce corrections due to the internal structure of the proton, this experiment will measure Q_w^p at low momentum transfers between the scattered electrons and the proton target ($Q^2 = 0.03(GeV/c)^2$). As mentioned above, Q_{weak} uses parity-violating electron scattering to measure Q_w^p. In

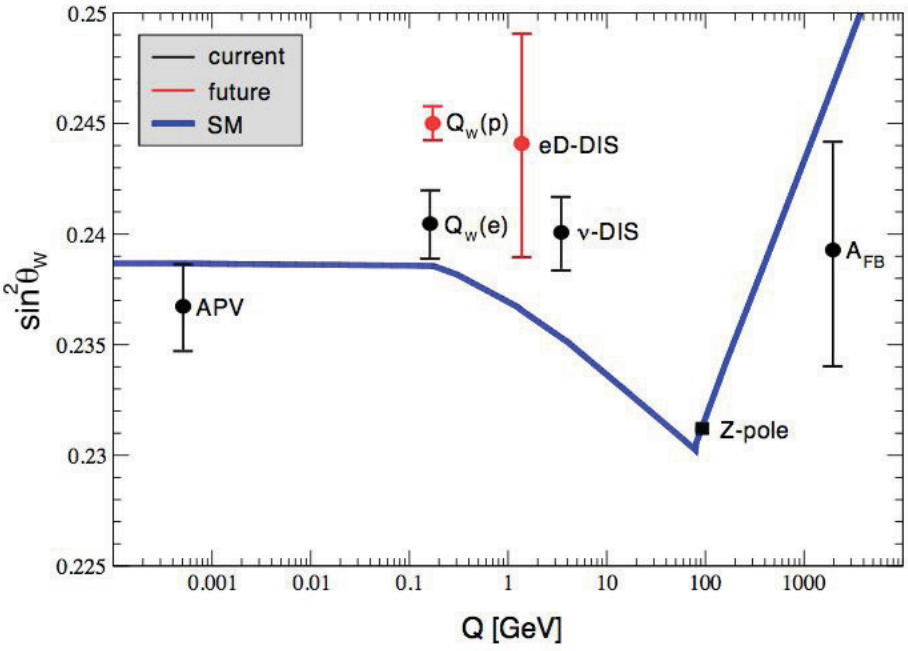

Figure 2.4: Running of $\sin^2(\theta_w)$: This image shows the value of $\sin^2(\theta_w)$ as a function of energy. The Standard Model(SM) prediction is indicated by the blue line. Existing measurements [7,8,9,10] with corresponding error bars are shown in black. The red points indicate future measurements and are placed at an arbitrary location with respect to the vertical axis. Error bars for these points indicate the anticipated uncertainty in the measurement.

particular, the scattering cross section for right- and left-handed elastically scattered electrons will be measured. Using these quantities, we can define an asymmetry in elastic scattering as,

$$A_{LR} = \frac{\sigma_L - \sigma_R}{\sigma_L + \sigma_R}, \tag{2.2}$$

where σ_L and σ_R are the scattering cross sections for left- and right-handed electrons, respectively. It can be shown from electroweak theory [6] that this asymmetry can also be written as an expansion in Q^2, given by

$$A_{LR} = \frac{1}{P}\frac{-G_F}{4\pi\alpha\sqrt{2}}[Q_w^p Q^2 + B_4 Q^4 + ...]. \tag{2.3}$$

Here, P is the polarization of the incident electron beam, G_F is the Fermi coupling, α is the fine structure constant, and B_4 contains form factors describing the proton structure. From this equation, it is evident that for low Q^2, we can ignore the higher order terms(Q^4, Q^6, ...). Thus, we are left with an equation relating the proton's weak charge to the asymmetry in scattering cross section, and other known and measureable quantities.

2.5 Experimental Setup

In the Q_{weak} experiment, a 180 μA electron beam at 1.16 GeV with 85% polarization is focused onto a 35 cm liquid hydrogen target. A series of lead collimators is then used to select only electrons with a scattering angle of $9^\circ \pm 2^\circ$, corresponding to a Q^2 of 0.03 $(GeV/c)^2$. A large toroidal magnet is then used to further select only electrons that have scattered elastically.

These elastically scattered electrons are focused onto a set of eight quartz Cerenkov detectors, while electrons that have scattered inelastically are bent away from the Q_{weak} apparatus. A schematic of the experimental setup is shown in Figure 2.5 [6].

As the name implies, the Cerenkov detectors work on the principle of Cerenkov radiation. When charged particles (scattered electrons in this case) travel through a material faster than the speed of light in the medium, atoms within the material become excited. These atoms quickly return to their ground state and, consequently, emit radiation in the process. In Q_{weak}'s Cerenkov detectors, this radiation is emitted in the form of visible and UV light (photons). Photomultiplier tubes are connected to the ends of the detectors and detect the emitted photons. Data from these detectors will be used to determine the scattering cross sections. In order to obtain results for both right- and left-handed electrons, the beam polarization will be continuously reversed at rates up to 960 Hz.

2.6 Tracking System

Data for the Q_{weak} experiment will be taken in two separate modes. In production mode, the full 180 μA current will be employed, and the asymmetry in scattering will be measured. Periodically, the beam current will be reduced to run the experiment in tracking mode. From equation 2.3, it is evident that to make a precision measurement of Q_w^p, the momentum transfer, Q^2 must be accurately determined. For these measurements, a dedicated tracking system has been installed in the Q_{weak} apparatus, and is labeled by Regions 1,2, and

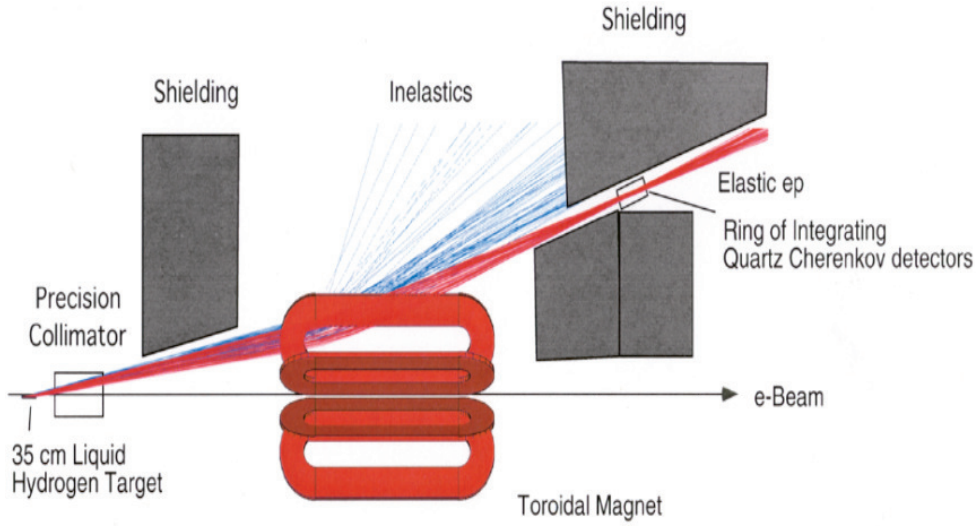

Figure 2.5: Basic Layout of Q_{weak} Experiment: This image gives a side view of The Q_{weak} Experiment. After the electron beam scatters off the liquid hydrogen target, a series of collimators and the QTOR magnet select out only the electrons that have elastically scattered with $Q^2 = 0.03\ (GeV/c)^2$. These electrons are focused onto the quartz Cerenkov detectors.

3 in Figure 2.6 [6].

For elastic scattering, it can be shown [6] that

$$Q^2 = \frac{4E^2 \sin^2(\frac{\theta}{2})}{1 + 2\frac{E}{m_p}\sin^2(\frac{\theta}{2})}. \tag{2.4}$$

Here, E is the incident beam energy, θ is the scattering angle, and m_p is the mass of a proton. The incident beam energy will be measured using the existing energy measurement system at Jefferson Lab. Thus, to calculate Q^2, we are left with the task of determining the scattering angle. The Q_{weak} tracking system is used to determine this scattering angle, and to ensure that equation 2.4 is valid, by confirming that the electrons did indeed scatter elastically.

The tracking system consists of three regions. Each of these regions will measure the position of scattered electrons at different points within the Q_{weak} apparatus. Region 1 consists of gas electron multiplier chambers, and measures the position of electrons immediately after they scatter off the hydrogen target. Region 2 consists of horizontal drift chambers, and measures the position and angle of scattered electrons immediately before they enter the toroidal magnet. Together, Regions 1 and 2 are used to determine the electrons' scattering angle. Region 3 measures the position and angle of scattered electrons after they exit the QTOR magnet and before they enter the Cerenkov detectors. This measurement will be used to determine the momentum of scattered electrons, to ensure these electrons were scattered elastically.

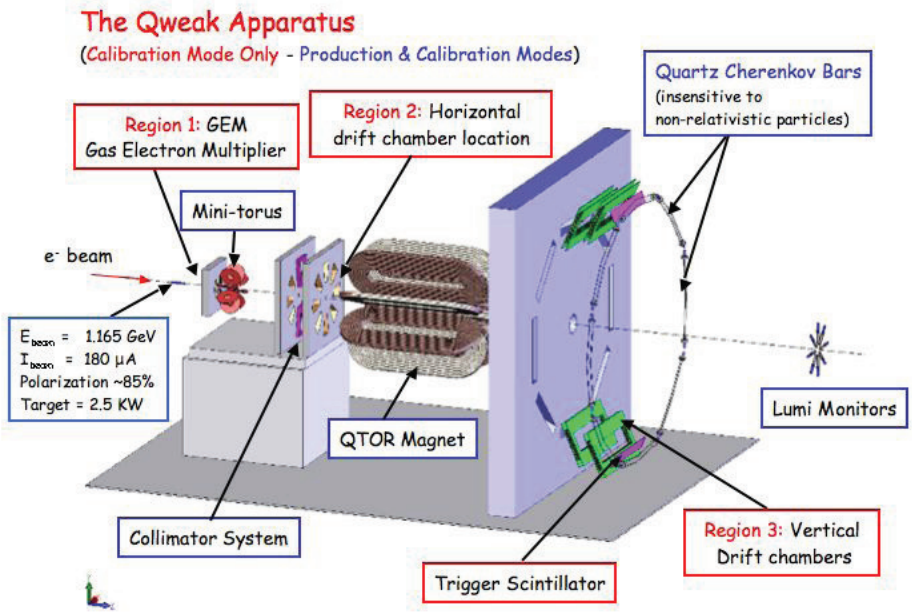

Figure 2.6: Detailed Layout of Q_{weak} Experiment: Here, we see a layout of the Q_{weak} apparatus, including the tracking system. The tracking system is labeled by Regions 1, 2, and 3. The mini-torus, shown here, is not used.

2.7 Region Three Drift Chambers

Region 3 consists of four vertical drift chambers (VDCs)[1] that track the motion of scattered electrons after they exit the QTOR magnet. These four chambers are separated into pairs of two[2], each of which are placed on opposite ends of a large rotator. During individual tracking runs, data is recorded for only two octants of the experimental apparatus at a time. To cover all eight octants, multiple data runs are taken, and the rotator is moved to a new position between runs. This rotator system reduces the number of drift chambers necessary for the experiment, but does require more beam time than if chambers were built to cover all eight octants at once.

A drift chamber is a type of wire chamber, used to detect charged particles. It consists of multiple wire planes and high voltage planes, contained in a gas mixture. The Region 3 drift chambers each contain two wire planes and three high voltage planes, and use an argon-ethane gas mixture (50% Argon/50% Ethane). On each wire plane, 280 gold-plated tungsten wires with diameter 25 μm are strung at an angle of 26.5° degrees with respect to the long side of the chamber. The perpendicular spacing between each of these wires is 0.5 cm. The wire planes in each chamber are oriented with respect to one another such that the wires form a "criss-cross" pattern, or grid (see Figure 2.7 [11]). This grid defines a coordinate system that is able to localize the position of a particle passing through the chamber.

[1]The four chambers are each given individual names. These are Vader, Leia, Han, and Yoda.

[2]These pairs are denoted as Package 1 and Package 2. Package 1 includes Vader and Leia; Han and Yoda are in Package 2.

2.7.1 Particle Detection

During the experiment, an approximate voltage of -3800V is applied to each of the high voltage planes, and the wires are held at ground. This sets up a large electric field between the wires and the voltage planes. When a scattered electron passes through the drift chamber, it collides with the gas molecules, causing the ionization of some (mostly) argon molecules. The free electrons produced from this ionization are repelled from the negative high voltage planes, and consequently, accelerate (or drift) towards the wires, which are held at ground potential. Close to the wires, the density of the electric field lines increases, resulting in a field enhancement. Because of this field enhancement, the closer the electrons drift towards the wires, the greater their acceleration. This rapid acceleration results in the ionization of even more molecules. The net effect is a large number of ionized electrons reaching the grounded wires, and is known as the avalanche effect. To prevent spontaneous and unwanted avalanches due to secondary emissions, ethane is included in the gas mixture as a quenching agent. Its polyatomic structure allows it to absorb photons produced during an avalanche, without emitting additional electrons. Upon reaching one of these wires, the free electrons induce a signal (or hit) in the wire. This signal is read out by a system of electronics to determine the relative timing of the hit. Using a time-to-distance algorithm[3], the drift distance for the original ionized electron can then be determined from the relative timing of this hit. In the experiment, each scattered electron will produce hits on multiple wires in

[3]The gas mixture used results in an approximately constant drift velocity, thus simplifying the time-to-distance algorithm.

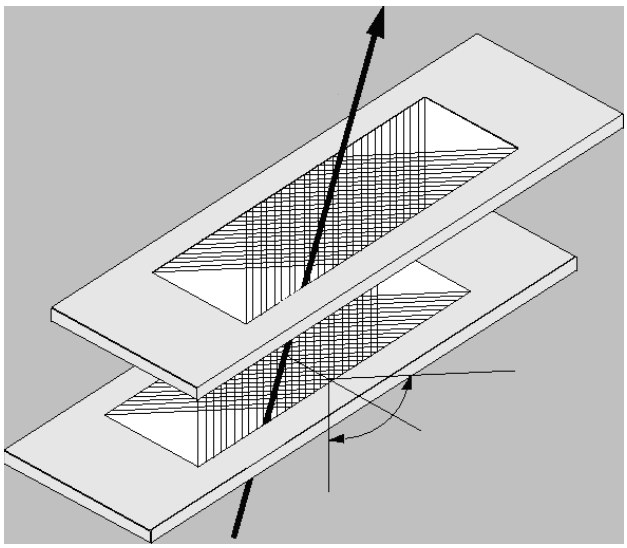

Figure 2.7: Chamber Geometry: The thick black arrow represents the path of a scattered electron as it passes through two drift chambers(one package). In this image, the grid, formed from the "criss-cross" orientation of the wire planes, can be seen. *Note: Distances and angles not drawn to scale.

each wire plane. The closer a scattered electron passes by a given wire, the smaller the corresponding drift time (and drift distance). By analyzing these drift distances for each wire, the position and angle of the scattered electrons can be reconstructed.

2.7.2 Data Acquisition

After the ionized electrons induce a hit in each of the wires, a sophisticated system of electronics reads out and records the data. Each wire is connected to one channel of an amplifier/discriminator circuit board. For each chamber, there are 36 of these circuit boards (known as MAD boards [12]). These circuit boards have an adjustable threshold voltage. Only wire signals whose magnitude is greater than this threshold voltage register hits on these MAD

boards. The output of these MAD boards is a low voltage differential signal (LVDS) for each wire, and these signals are carried by twisted pair wires. The next step in the data collection sequence is to convert these LVDS signals into data that can be stored, manipulated, and analyzed on a computer. For this, the LVDS signals are fed into a time to digital converter (TDC). These TDCs turn an analog signal pulse into a digital representation of the time each wire received a hit. Since the total number of wires in all four of the VDCs is 2240, it would require 35 64-channel TDCs to handle the experimental data. To reduce this expense, a multiplexing system [13] was implemented to reduce the number of required TDCs to just four. In this multiplexing system, the signals of 18 wires from separated regions of the chambers are fed into two TDC channels along delay lines. The individual wires are then identified by the difference of the two signals, and the drift time can be extracted by taking the sum of the two signals. Concurrently, trigger signals are sent to the TDC from the trigger scintillators located in front of the drift chambers. The signals from these scintillators indicate when chamber data should be recorded, as well as provide a reference time for the wire pulses. This entire data acquision process is shown conceptually in Figure 2.8 [13]. All of the wire data recorded for a single scintillator trigger is collectively referred to as an event. These scintillators are used to reduce any noise that may make its way onto the chamber wires. Data from the TDCs are then stored on a computer, where it can be manipulated and analyzed using the ROOT [14] data analysis framework.

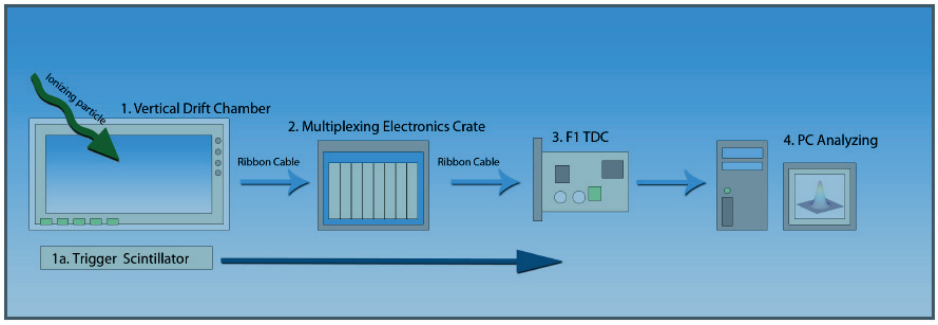

Figure 2.8: Data Collection Sequence: This sequence chart gives a conceptual overview of the data acquisition process.

2.7.3 Data Analysis

Raw data from each Q_{weak} tracking run is stored as a file on the Jefferson Lab computing system. This raw data is then processed by the Q_{weak} analyzer (essentially a data analysis program), and the output is a new data file (root file) that can be analyzed inside the ROOT data analysis framework. Within each root file, tracking data is organized by event number. For every event, we can extract information about each hit in that event. This information includes package number, wire plane number, wire number, drift time, and drift distance for each hit. In addition to recording and organizing this basic information, the analyzer also searches through the data file and looks for track candidates. A track candidate is an event where the drift distances on consecutive wires are likely to represent the path of a scattered electron. These events are characterized by a linear relationship between drift distance and wire position. Within ROOT, these events are labeled as "tree lines". If tree lines on multiple wire planes can be meshed together to fit the path of scattered electron, this is referred to as a "partial track". Partial tracks from

Regions 1, 2, and 3 are used to reconstruct the complete track of a scattered electron.

Table 2.1 shows drift distances for each wire in a typical tree line candidate event. These points are plotted in Figure 2.9, where the linear relationship can be seen. Just as with individual events, the root file contains useful information about both tree lines and partial tracks. For each of these quantities, we can determine the wires involved (including which plane(s) and package), the direction and slope of the fitted line, and the average residual between the drift distance and the fitted line. ROOT is then able to make histograms of this data, to look at general trends for entire data runs. The results presented in this paper were obtained by analyzing ROOT data for a variety of tracking runs.

Wire Number	Drift Distance (cm)
101	1.17
102	0.58
103	-0.09
104	-0.57
105	-1.23

Table 2.1: Here we see drift distances for each wire in a typical tree line candidate event. When plotted the linear relationship between wire number and drift distance can be seen.

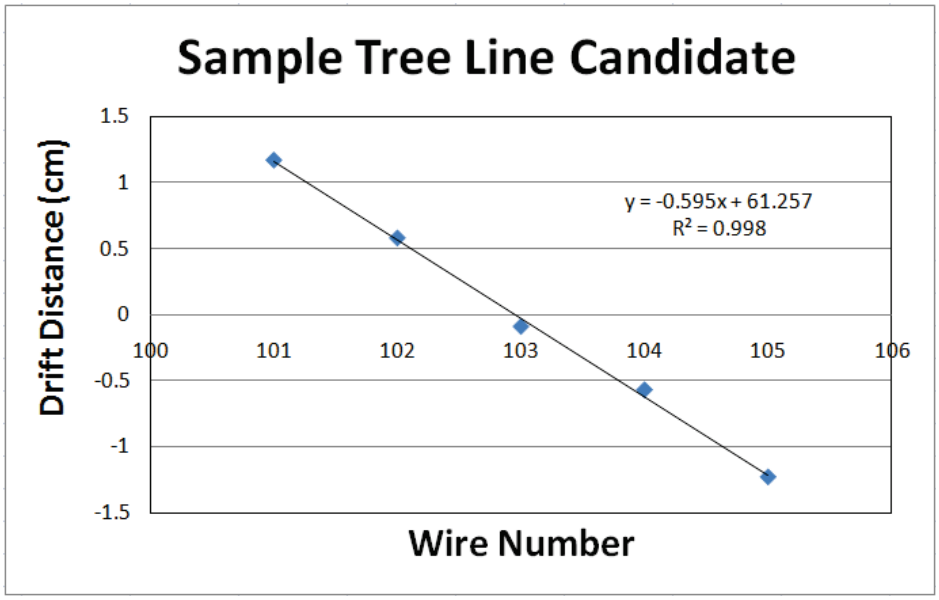

Figure 2.9: Tree Line Candidate: Here, we see a plot of the data points given in Table 2.1. The linear relationship between wire number and drift distance can be observed, and therefore, this event is likely to be interpreted as a tree line candidate by the Q_{weak} tracking analyzer.

Chapter 3

Measures of Chamber Performance

The purpose of the research presented in the subsequent sections is to provide a quantitative analysis of Region 3 VDC performance variations with running conditions. Since Q_{weak} seeks to make a precision measurement of Q_w^p, experimental error should be kept to a minimum. Optimizing the performance of all components of the Q_{weak} apparatus will help to keep the combined systematic and statistical error in the measurement at or below 4%.

As evident in equation 2.3, an accurate measurement of Q^2 is a vital ingredient in the determination of Q_w^p. The ability of the Region 3 drift chambers to track electrons will factor into this Q^2 measurement. However, an exact (mathematical) relationship between VDC performance and uncertainty in Q^2 is not available. This is due to the fact that a closed form solution of the toroidal magnetic field does not exist. Therefore, projections of tracks from

Regions 1 and 2 to Region 3 are based on computer simulations. This means that exact relationships between VDC performance and the uncertainty in Q^2 must be determined empirically. At present, data are not available to precisely determine these relationships. Nonetheless, we can infer that optimizing the performance of the Region 3 VDCs will minimize the uncertainty in the Q^2 measurement. The research discussed below seeks to find the optimal running conditions for the Region 3 VDCs. Three measures of chamber performance are discussed, and results with respect to beam current, VDC high voltage, and VDC threshold voltage are presented.

3.1 Relative Tracking Efficiency

One method for measuring the efficiency with which the VDCs can detect electron tracks is to compute the relative tracking efficiency. This measure of efficiency analyzes the performance of each entire VDC package by comparing the number of partial tracks found in a given data run to the total number of trigger scintillator TDC hits in that run. Mathematically, the relative efficiency is calculated by,

$$E_{rel} = \frac{n_{pt}}{n_{f1}}, \tag{3.1}$$

where n_{pt} and n_{f1}[1] are the total number of partial tracks and TDC hits, respectively. In any given data run, there will be more TDC triggers than partial tracks. This is partly due to ambient noise[2] in the experimental

[1] "f1" refers to the specific TDC that is used for Region 3.
[2] Including low-energy radiation present in the experimental hall.

hall, and partly because the VDCs will not detect every scattered electron. For this measure of performance, we are concerned with quantifying the percentage of electron tracks that the VDCs detect. However, because there is no way to distinguish the trigger scintillator signals due to noise from those due to real electron tracks, we are forced to include both types of these signals in our relative efficiency calculation. What this means, is that this relative efficiency will be lower than the actual chamber efficiency. Consequently, these results are useful for comparing chamber performance in a series of consecutive data runs (where the level of ambient noise should be constant), but care must be taken when comparing tracking data from different series of runs[3]. Since we are assuming a constant level of noise in consecutive data runs, any variation in the VDC relative efficiency should be due to performance variations of the chambers, themselves.

To compare relative efficiency data from separate series of tracking runs, we must introduce a scaling factor, λ. For data taken with the same VDC running conditions (HV and threshold) in two separate data runs (from different run series), λ may be calculated. For these two data runs, we assume that the chambers should have a similar level of performance, and that variations in the relative efficiency between these data runs are due to external factors (noise, beam current, etc.). We then arbitrarily choose one of these data runs, and calculate the relative efficiency of the VDCs. Let us denote this efficiency as $E_{rel_{base}}$. We will denote the efficiency of the other data run as $E_{rel_{scale}}$. The scaling factor is then defined as

[3]Tracking runs are executed periodically. For runs taken weeks (or months) apart, the level of ambient noise will vary.

$$\lambda = \frac{E_{rel_{base}}}{E_{rel_{scale}}}. \tag{3.2}$$

The relative efficiencies in the second series of data runs are then multiplied by λ to obtain the scaled relative efficiencies for that run series. The relative efficiencies between these two series of data runs can then be compared, and relationships in data can be inferred.

3.2 Five Wire Efficiency

A second measure of chamber performance is the five wire efficiency, which looks at the ability of individual wires to detect particle tracks. For an individual wire, we can define an efficiency in the following way. We let t_i denote the total number of triggers for the i^{th} wire. Here, a trigger is defined as a set of conditions that define when an individual wire should have registered a hit. We let h_i denote the total number of successful hits on a given wire. A successful hit means that all trigger conditions for the i^{th} wire were met, and that wire registered a hit. The efficiency for the i^{th} wire is then given as,

$$E_{wire_i} = \frac{h_i}{t_i}. \tag{3.3}$$

In general, we are not concerned with the efficiency of one particular wire at a time; we are concerned with how these individual wire efficiencies change with running conditions. To investigate this behavior, we compute a weighted sum of the efficiencies of all individual wires in a given plane (or

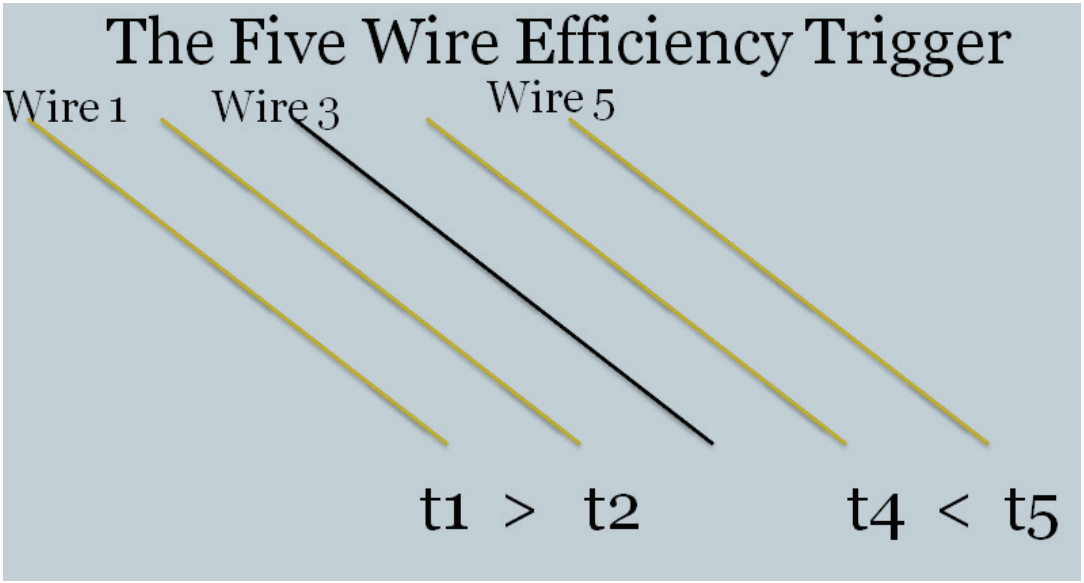

Figure 3.1: Five Wire Efficiency Trigger: Here we see the trigger conditions for the five wire efficiency of Wire 3. Wires 1, 2, 4, and 5 must all register hits. Additionally, the drift distance for Wire 1 must be greater than that for Wire 2, and the drift distance for Wire 5 must be greater than that for Wire 4. For a successful fire, the same conditions are required, in addition to Wire 3 registering a hit.

chamber, or package). This total plane efficiency is given by,

$$E_{plane} = \frac{\sum_i h_i}{\sum_i t_i} \tag{3.4}$$

Here, $\sum_i$ sums over all the wires in a given plane. Similarly, to calculate $E_{chamber}$ and $E_{package}$, we choose indices for all relevant wires for that sum. In the five wire efficiency test, a trigger for Wire i requires that both pairs of wires immediately adjacent to Wire i register a hit. However, because we only want this efficiency test to measure a wire's performance in detecting tracks, we place stronger conditions on these triggers. Table 2.1 shows drift distances for a likely track candidate. We want our five wire efficiency triggers to select out events of this type. Thus, we require that the drift distance for Wire $i-2$ to be greater than the drift distance for Wire $i-1$. Similarly, we require the drift distance for Wire $i+2$ to be greater than the drift distance for Wire $i+1$ [4]. If both of these conditions are met, a trigger is registered for Wire i. A successful fire for Wire i occurs when both of these trigger conditions are met and Wire i registers a hit. After finding the total number of triggers and successful fires in a given data run, the five wire efficiency can be calculated from equation 3.3 (for an individual wire) or equation 3.4 (for a collection of wires).

[4] In a ROOT file, all drift distances are given as positive values. The tracking software determines which drift distances should be negative by finding the combination that best fits tree lines into partial tracks.

3.3 Mean Average Residual

Thus far we have seen two measures of chamber performance that address how well the VDCs can detect scattered electrons. Another measure of chamber performance analyzes how well the chambers and tracking software can reconstruct a particle track once it has been found. After a scattered electron exits the QTOR magnet, it is no longer subjected to forces that alter its direction of motion. Thus, the scattered electrons should follow a linear trajectory through the VDCs and into the Cerenkov detectors. For this reason, we expect the Region 3 VDCs to detect straight-line particle tracks. The tracking software is programmed to look for these straight-line tracks. For these tracks, a linear regression model relating wire position to drift distance can be fit to the data points. One method for evaluating how well these linear regression models fit the data points is to compute the residual for each point. For each data point, the corresponding residual is a measure of its distance from the linear regression fit. In other words, it is the error between the actual drift distance, and the drift distance predicted by the linear regression fit. For an individual data point, a large residual indicates the linear regression model is not an accurate representation of that data point. For a collection of data points and the corresponding linear regression fit, we can consider their average residual. This average residual is given by the sum of the magnitude of the individual residual values, divided by the total number of data points. It is a measure of how well the linear regression model fits the data set.

For the VDCs, the average residual is a measure of the resolution with

which we can reconstruct particle tracks. A large average residual would mean that the scattered electron passed closer or farther from the individual wire than the model indicates. This means that we cannot be sure that the linear regression fit gives an accurate reconstruction of the particle path. To account for this uncertainty, we must include an associated error in the eventual calculation of Q^2. A small average residual indicates that the data points closely follow a linear relationship. Because this is what we expect, a small average residual allows us to infer that the drift distances are giving an accurate measurement of the particle position. Consequently, for tracks with small residuals, there will be a smaller associated error in the calculation of Q^2.

To evaluate the performance of the VDCs in reconstructing electron tracks, we look at residuals for fitted tree lines. For an individual tree line, the average residual of all data points is calculated. We then use ROOT to make a histogram of all the average residual values in a given tracking run, and to calculate the mean of these average residuals for all tree lines in that run. These mean average residuals[5] can then be plotted with respect to each of the operating parameters, to determine which set of conditions gives the best track reconstruction.

[5]The term "mean average residual" may sound redundant. It is important to remember that we are taking the mean of a collection of values, where the values are the average residuals for individual tree lines.

Chapter 4

Results

The results presented in this chapter are based on data from two series of tracking runs. The first series of these runs took place over the course of a few days in January 2011, and provide the majority of data used in the subsequent analysis. Data from this series includes threshold, high voltage, and beam current studies. The second series of tracking runs took place over a few days in March 2011, and provides additional high voltage data to supplement the January runs. Other tracking runs in March 2011 were used to study the behavior of other components of the tracking system, and to provide initial measurements of Q^2. Table 4.1 lists the relevant tracking runs for the VDC performance analysis, and gives the corresponding operating conditions for each run.

Run Number	Beam Current	High Voltage (V)	Threshold Voltage* (V)
8628	50 pA	3800	8.0
8629	50 pA	3700	8.0
8630	50 pA	3600	8.0
8631	50 pA	3900	8.0
8632	50 pA	3800	7.0
8633	50 pA	3800	6.0
8634	50 pA	3800	9.0
8635	50 pA	3800	10.0
8710	1.7 nA	3800	8.0
8713	10 nA	3800	8.0
8714	20 nA	3800	8.0
8715	30 nA	3800	8.0
10644	50 pA	3820	8.0
10645	50 pA	3720	8.0
10646	50 pA	3620	8.0
10647	50 pA	3520	8.0
10648	50 pA	3420	8.0
10649	50 pA	3320	8.0
10650	50 pA	3220	8.0
10651	50 pA	3120	8.0

Table 4.1: This table lists the tracking runs that provide the data presented in this paper. Runs 8626-8715 were taken in January 2011 and provide data for high voltage, threshold voltage, and beam current studies. Runs 10644-10651 were taken in March 2011 and supplement the January high voltage studies. Note: High Voltage and Threshold Voltage refer to the Region 3 operating conditions.
*These are not the actual threshold values. These are the voltages supplied to the MAD board threshold input, and are proportional to (but much larger than) the actual threshold voltages.

4.1 High Voltage Studies

The Region 3 VDCs each contain three high voltage planes. The voltage applied to these planes directly affects the electric field inside the drift chamber. Higher voltages induce higher electric fields. Consequently, the primary ionized electrons will experience a greater acceleration towards the grounded wires for higher voltages. This will lead to more secondary ionizations as these electrons collides with other gas molecules (greater avalanche effect), thus inducing a larger pulse height in the wires. The effect is that for higher voltages, scattered electrons should be easier to detect. At the same time however, a higher voltage means that more noise (other particles, secondary emissions, etc.) will produce signals on the VDC wires. Therefore, optimizing the high voltage requires balancing signal detection with noise reduction. The results in this section aim to find this optimal level of high voltage.

4.1.1 Relative Tracking Efficiency

Relative tracking efficiencies were calculated for runs 10644-10651 (March) and runs 8628-8631 (January). In the March set of tracking runs, the beam current was fixed at 50 pA, and the VDC threshold voltage was held constant at 8.0 V. VDC high voltage started at 3820 V, and was lowered by 100 V between each tracking run. For the January tracking runs, beam current and threshold voltage were identical to the March runs, but the high voltages ranged from 3600 V to 3900 V (in steps of 100 V). Figure 4.1 plots these relative efficiencies vs. high voltage. In this graph, the January efficiencies are scaled to the March efficiencies. Relative efficiencies from runs 10644 and

8628 were used to calculate the scaling factors, λ.

In Figure 4.1, we see a clear relationship between high voltage and efficiency. Below 3400 V, the chambers are not operational, as they failed to find any tracks. Between 3400 V and 3700 V, an increase in high voltage corresponds to an increase in relative chamber efficiency. In this voltage range, the chambers are operational, but are not operating at their maximum efficiency. Above 3700 V, the efficiency reaches a plateau. In this voltage range, an increase in high voltage does not correspond to an increase in relative efficiency. This plateau suggests that for tracking runs, the VDC high voltage should be at least 3700 V. However, from this graph, a single optimal voltage cannot be inferred. According to this measure of performance, there is no difference between operating at 3700 V vs 3900 V. To determine if VDC performance varies with high voltage above 3700 V, we will have to look at the other measures of chamber performance.

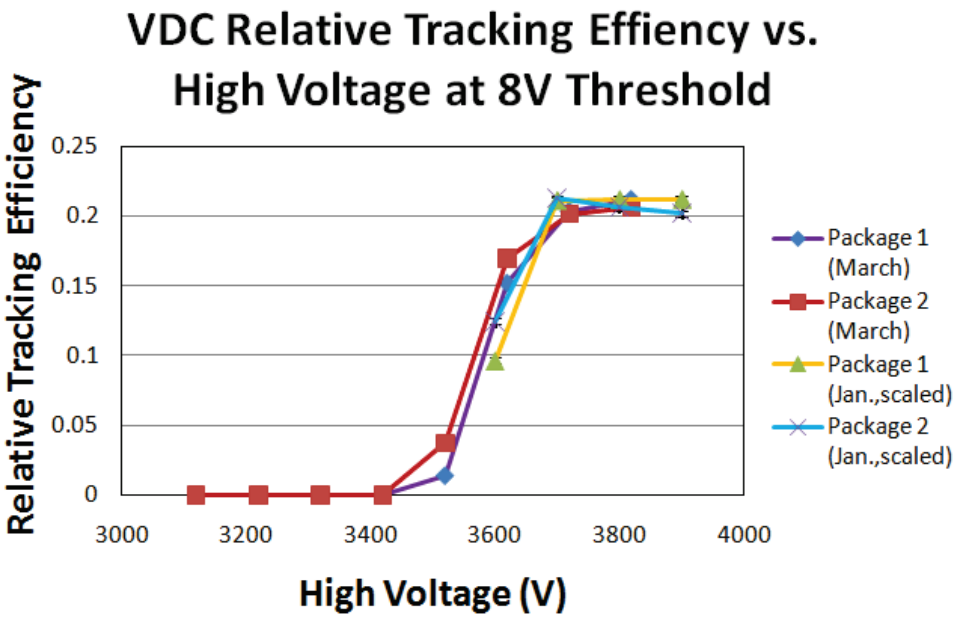

Figure 4.1: Relative Tracking Efficiency vs. High Voltage: This graph plots VDC relative tracking efficiency as a function of high voltage. Data are included from the January and March 2011 tracking runs. The January data have been multiplied by a scaling factor, so that we may compare these two sets of data on the same graph.

4.1.2 Five Wire Efficiency

Results from the previous section indicate that the VDCs operate at optimal relative efficiency for high voltages at or above 3700 V. This section looks at the five wire efficiency of the VDCs in this voltage range. Five wire efficiencies were calculated individually for each VDC according to equation 3.4, and results are shown in Figure 4.2.

In this graph, we see that for chambers Vader, Leia, and Han, the five wire efficiency follows the same trend as the the relative efficiency. Between 3600 V and 3700 V, there is a significant increase in the five wire efficiency. After this increase, the efficiency reaches a plateau for voltages at/above 3700 V. In this range, changes in high voltage do not correspond to changes in five wire efficiency. Therefore, based on the data presented in this section, there is an optimal range of high voltages at which the chambers can operate. However, we still have not determined if a single high voltage optimizes chamber performance.

This graph also shows that the behavior of the Yoda chamber differs from the other three VDCs. Unlike the other three chambers, the Yoda chamber does not reach an efficiency plateau for the five wire efficiency measure. Yoda obtains a maximum efficiency at 3700 V, and this efficiency begins to decline for higher voltages. Further research is needed to understand this different behavior of the Yoda chamber.

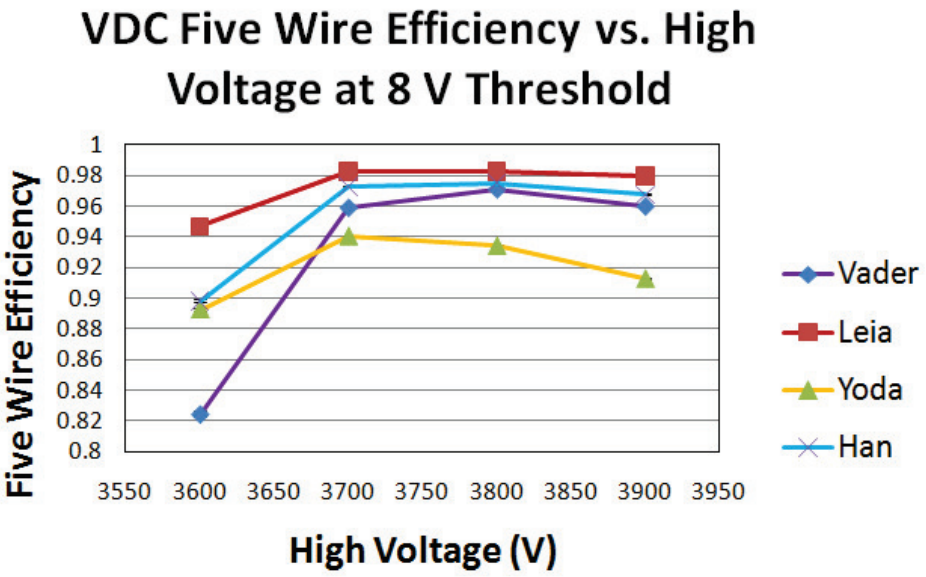

Figure 4.2: Five Wire Efficiency vs. High Voltage: Here, the five wire efficiency of each drift chamber is plotted as a function of high voltage for the January 2011 tracking runs.

4.1.3 Average Residual

In this section, we look at how the average residual of tree lines changes with high voltage. Data are included from both the January and March 2011 tracking runs. In this analysis, we looked at residuals from two types of tree lines. The first is a tree line within one single wire plane. In Figure 4.3, this data series is labeled "P!=0." The other data series is labeled "P=0." If the tracking software is able to connect two tree lines from different wire planes, the plane for this new tree line is given the value 0. This system is used to differentiate tree lines in a single wire plane from those that are formed in multiple wire planes.

Figure 4.3 plots the relationship between mean average residual and VDC high voltage. We see that, between 3300 V and 3700 V, average residual decreases with increasing voltage. This suggests that for optimal performance, results from these residual studies are consistent with results from both efficiency measures. The applied high voltage on the chambers should be at least 3700 V. For single-plane tree lines, the mean average residual levels off for voltages above 3700 V. However, for multi-plane tree lines, the mean average residual increases as the voltage is increased to 3900 V. Without more data, it is unclear whether this is a trend that will continue. Nonetheless, based on the data available, we can conclude that the chambers should be operating at voltages near 3700 V and 3800 V.

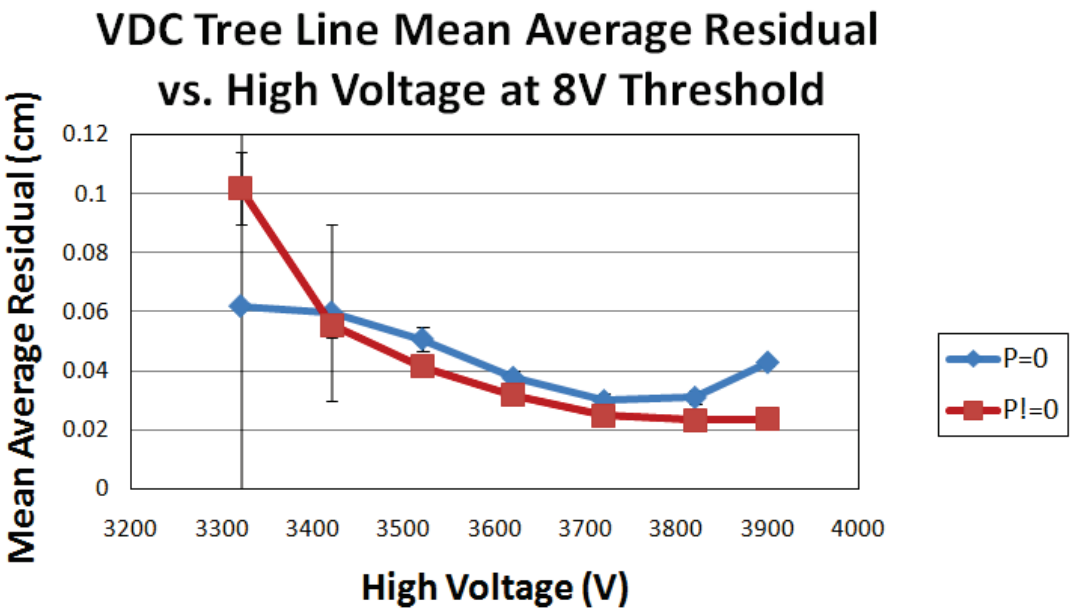

Figure 4.3: Mean Average Residual vs. High Voltage: In this plot, the mean average residual of tree lines is plotted vs. high voltage. "P!=0" indicates tree lines that exist in one single wire plane. Tree lines that include data points from two or more wire planes are given the label "P=0."

4.1.4 Discussion

These results indicate that the Region 3 VDC performance depends on the applied high voltage. In all three performance measures, the best results were obtained for voltages at and above 3700 V (for 8.0 V threshold). For both the relative and the five wire efficiency measures, the calculated efficiency reached a plateau at 3700 V. Below this voltage, there are some electron tracks that are not detected by the VDCs. This is because at these lower voltages, the electric field does not provide a sufficient acceleration to the ionized electrons. Consequently, there is a much smaller avalanche effect (or none at all), and the signals produced in the wires are smaller than the MAD board threshold voltage. Once the applied voltage reaches 3700 V, the electric field in the chambers is sufficient to induce avalanches for most of Q_{weak}'s elastically scattered electrons. Above this voltage, efficiency results did not correlate with changes in high voltage. The exception is for the Yoda chamber, where the five wire efficiency decreased with increasing voltage, for voltages above 3700 V. It is unclear why this behavior was observed, and more data may be needed to confirm this trend.

For the high voltage residual studies, we saw that the optimal chamber performance was obtained for voltages near 3700 V and 3800 V. Figure 4.3 shows that for these residual studies, data is included for voltages ranging from 3300 V to 3900 V. However, if we look at Figure 4.1, we see that below 3400 V, there were no partial tracks detected in these data runs[1].

[1]Average residuals were calculated for tree lines, not partial tracks. Thus, it is not inconsistent that we were able to calculate average residuals, despite there being no partial tracks. It simply means the tracking software was unable to connect any tree lines into partial tracks.

There are two possible explanations for this. First, the fits corresponding to electron tracks may be so poor that the tracking software is unable to combine tree lines into partial tracks. Second, the chambers may be detecting particles other than the experiment's scattered electrons, such as cosmic rays, or other sources of noise. The tracks of these particles are unlikely to have the necessary geometry to be detected by multiple wire planes. Therefore, partial tracks cannot be formed for these other particles. Since the chambers are not designed to detect these particles, we expect that track reconstruction for this noise will not be as accurate as it is for the scattered electrons. Once the chambers are on the efficiency plateau (3700 V), the ratio of signals to noise increases, and thus, the mean average residual at these voltages likely reflects the resolution with which scattered electron tracks can be reconstructed.

4.2 Threshold Voltage Studies

One step in the data acquisition process is determining which wire signals to record, and which signals to ignore. At any moment while the chambers are in operation, there is a certain level of electronic noise on the VDC wires. To prevent this noise from being recorded, the MAD boards have an adjustable threshold voltage. Wire signals smaller than this threshold voltage are ignored, while those above this threshold may be recorded. Therefore, this adjustable threshold needs to be large enough to keep these noise signals suppressed. If it is too high, however, some electron tracks may not be detected on certain wires. This section looks at how the VDC performance varies with this threshold voltage. Tracking data were recorded for threshold

voltages between 6.0 and 10.0 V, in 1 V increments. For these runs, there was a 3800 V high voltage applied to the chambers, and the beam current was fixed at 50 pA. Results for relative tracking efficiency, five wire efficiency, and residual studies are shown below.

4.2.1 Relative Tracking Efficiency

Figure 4.4 plots VDC relative tracking efficiency as a function of threshold. We see that for both packages, the relative efficiency tends to increase with increasing threshold. For Package 1 the relative efficiency increased by approximately 2%, and for Package 2 the relative efficiency increased by roughly 4.5% over the range of threshold values. This increase in relative efficiency with threshold voltage is not what is naively expected. In theory, a lower threshold means that more particles will be detected, thus increasing the number of partial tracks per TDC trigger. This will be addressed further in the discussion. Additionally, this graph shows that the Package 2 relative tracking efficiency is lower than that for Package 1. One possible explanation is that, despite the same threshold voltage being applied to all chambers, there exist some natural variations in the active threshold of the chambers. As suggested by this graph, a lower threshold for Package 2 compared to Package 1 may explain this disparity.

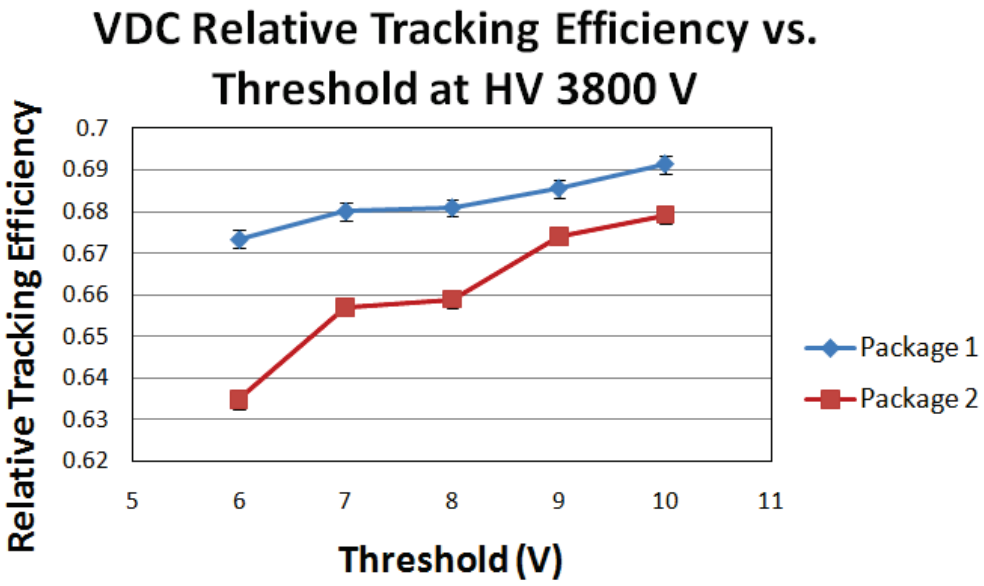

Figure 4.4: Relative Tracking Efficiency vs. Threshold Voltage: The graph shows the dependence of relative tracking efficiency on threshold voltage for Packages 1 and 2.

4.2.2 Five Wire Efficiency

The five wire efficiency of each VDC as a function of threshold voltage is plotted in Figure 4.5. From this graph, it appears there is a slight dependence of five wire efficiency on threshold voltage. The five wire efficiency increases with increasing threshold voltage. However, over the entire range of threshold values, the efficiency of three of the four chambers change by less than 1%. The exception is the Yoda chamber, whose efficiency increases by 2% over this range, but whose overall efficiency is well below the efficiency of the other three chambers. Again, this increase in efficiency with threshold voltage is not what is naively expected, and will be addressed in the discussion.

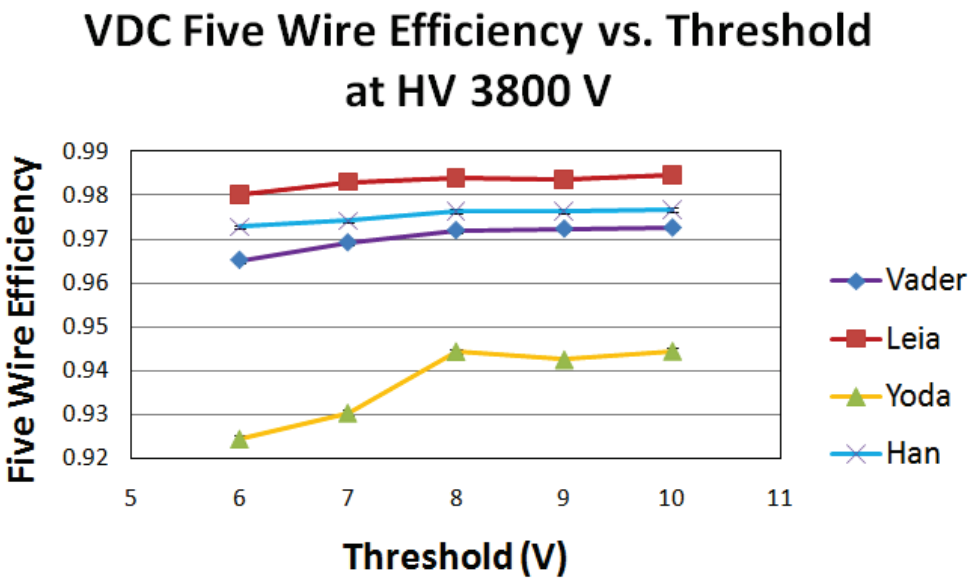

Figure 4.5: Five Wire Efficiency vs. Threshold Voltage: Here, the five wire efficiency of each chamber is plotted vs. threshold voltage.

4.2.3 Average Residual

Figure 4.6 shows the variation in VDC tree line mean average residual with threshold voltage. The results in this graph indicate that for single-plane tree lines, the mean average residual is not affected by the threshold voltage. For multi-plane tree lines, the mean average residual tends to slightly decrease with increasing threshold voltage. This suggests that higher threshold voltages have little effect on the amount of noise in any individual wire planes. However, for multi-plane events, the higher threshold voltages select track candidates with the best resolution, thereby reducing the mean average residual.

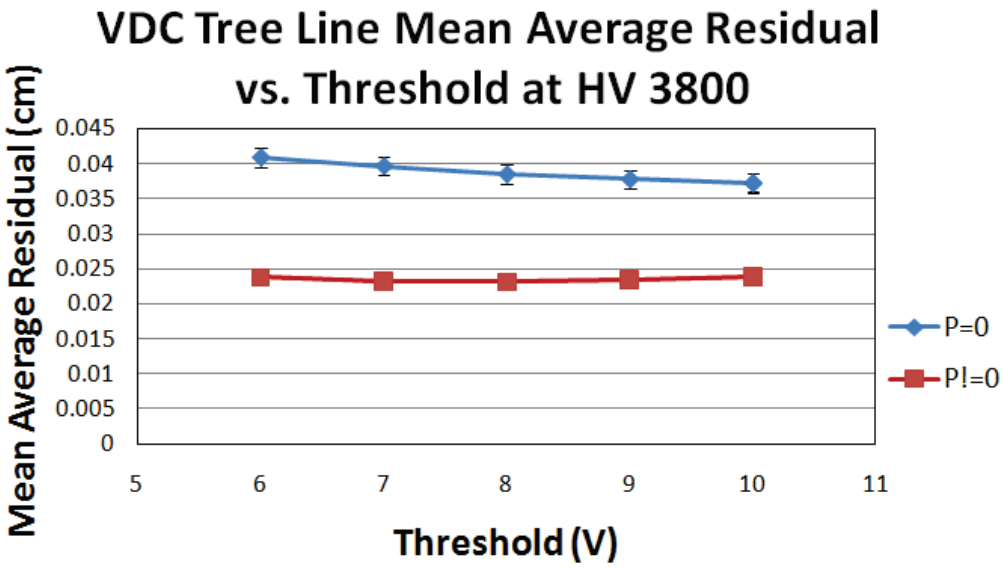

Figure 4.6: Mean Average Residual vs. Threshold Voltage: This graph shows the relationship between tree line mean average residual and threshold voltage. Results are shown for both single- and multi- plane tree lines.

4.2.4 Discussion

Results from this section provide evidence that increasing the MAD board threshold voltage optimizes Region 3 VDC performance. We saw that both measures of efficiency increase with increasing threshold. At the same time, the mean average residual for multi-plane tree lines decrease with increasing threshold. It was expected that increasing the threshold voltage would reduce the mean average residual. This is because higher threshold voltages filter out noise hits and signals that have the potential to negatively impact the mean average residual.

It was mentioned in the above sections that the observed relationship between efficiency and threshold is unexpected. The threshold voltage is designed to filter out noise signals that would dilute relevant chamber data. However, in the process of filtering these noise signals, the threshold will likely throw away smaller signals from actual electron tracks. For the relative efficiency measure, this would imply that some partial tracks, which would be detected at lower thresholds, are filtered out at higher thresholds. Since the number of TDC hits should be independent of the threshold voltage, we would expect the relative efficiency to decrease.

The fact that relative tracking efficiency increases with increasing threshold voltage may indicate that some noise signals are interfering with some relevant chamber signals. For each event, multiple hits are sometimes recorded for a single wire. Currently however, it is only the first hit that is used in the data analysis. Thus, if a relevant chamber signal is immediately preceded by a noise signal, the relevant signal may be excluded from the data analysis.

In this case, chamber performance would be optimized by using a higher threshold voltage.

For the five wire efficiency, we again saw that increasing the threshold voltage increases the chamber efficiency. One possible explanation is that the size of a wire pulse might be a function of how close the scattered electron passed to the wire. If electrons induce bigger pulses in the wires they travel closest to, then increasing threshold voltage would decrease the number of five wire efficiency triggers in a given tracking run. This is because the magnitude of smaller signals on Wires $i-2$ and $i+2$ would be less likely surpass higher threshold voltages. Therefore, we would expect more trigger conditions to fail than test conditions, thus increasing the five wire efficiency of the chambers. Further research is needed to support this explanation.

4.3 Beam Current Studies

During Q_{weak} tracking runs, the beam current is reduced from 180 μA (production mode current) to approximately 50 pA. However, because the current used in these tracking runs may not always be exactly 50 pA, a series of runs was taken to study the effects of beam current on VDC performance. Data for these runs were taken at beam currents ranging from 1.7 nA to 30 nA. These beam currents are significantly (order-of-magnitude) greater than the currents used in tracking runs. Nonetheless, they do provide a useful analysis of how beam current affects chamber performance.

4.3.1 Relative Tracking Efficiency

Figure 4.7 graphs VDC relative tracking efficiency vs. beam current. This graph shows that VDC relative efficiency decreases with increasing beam current. As the beam current increased from 1.7 nA to 30 nA, the relative efficiency of both packages decreased by approximately 7%. It is important to note, however, that these beam currents are significantly greater than those used in tracking runs. Therefore, we do not expect beam current variations to have a significant effect on VDC relative efficiency during these tracking runs. In Figure 4.7, we also see a difference in the relative tracking efficiency between Packages 1 and 2. However, this time (compared to Figure 4.4), the efficiency of Package 2 is greater than the efficiency of Package 1. This supports our assumption that this difference is due to natural variations in running conditions (such as threshold voltage).

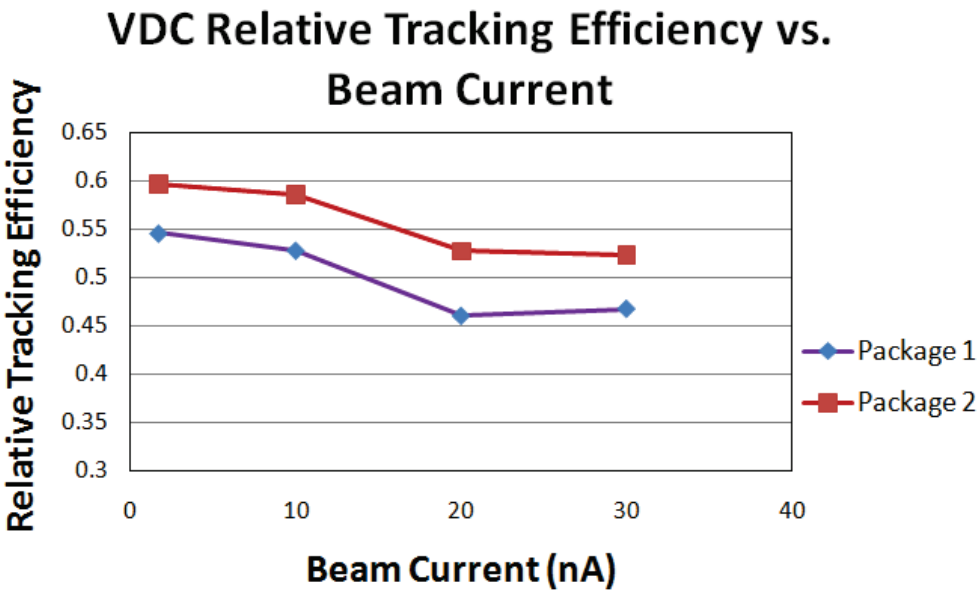

Figure 4.7: Relative Tracking Efficiency vs. Beam Current: The graph shows the dependence of relative efficiency on beam current. Results for Packages 1 and 2 are plotted separately.

4.3.2 Five Wire Efficiency

In Figure 4.8, we see a relationship between beam current and five wire efficiency. As with relative efficiency, the five wire efficiency also decreases with increasing beam current. Again however, the magnitude of beam currents for these studies is far greater than the currents used during actual tracking runs. Therefore, we do not expect the beam current variations during tracking runs to have a significant impact on the five wire efficiency of the chambers.

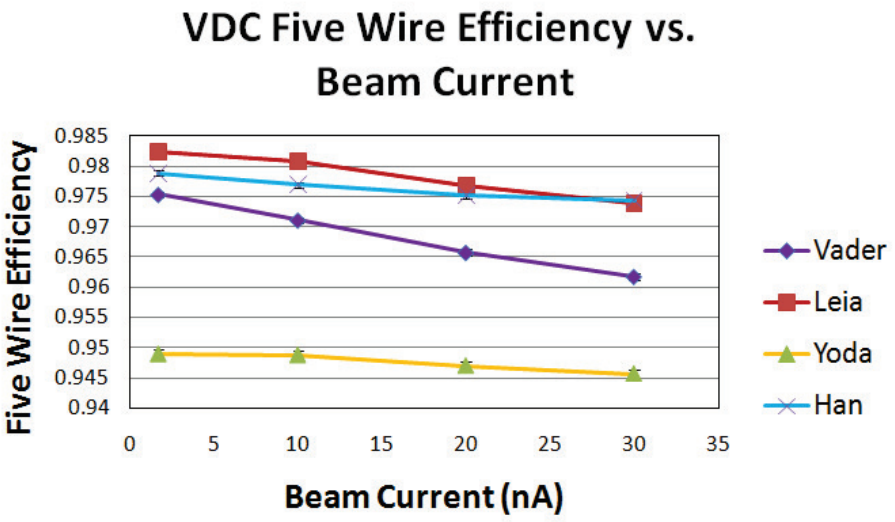

Figure 4.8: Five Wire Efficiency vs. Beam Current: Here, the five wire efficiency of each chamber is plotted vs. beam current. Data are from the January tracking runs.

4.3.3 Average Residual

The graph in Figure 4.9 plots mean average residual as a function of beam current. We see that for multi-plane tree lines, there does not appear to be a relationship between these quantities. There are some slight fluctuations in mean average residual for these multi-plane tree lines, but no definite relationship can be inferred. For single-plane tree lines, however, there does appear to be a small correlation between beam current and mean average residual. Mean average residual for these single-plane tree lines appears to increase slightly with increases in beam current. Again, we do not expect this effect to be significant at the beam currents used for Q^2 measurements.

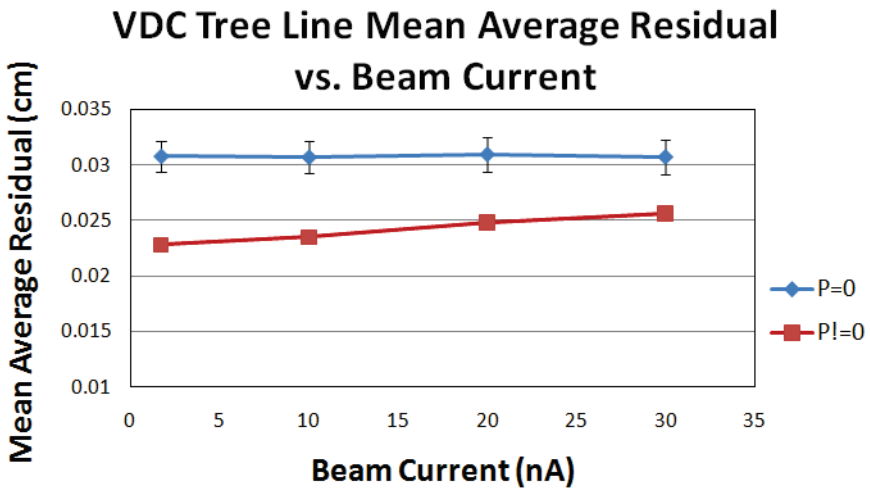

Figure 4.9: Mean Average Residual vs. Beam Current: This graph shows the relationship between tree line mean average residual and beam current. Results are shown for both single- and multi- plane tree lines.

4.3.4 Discussion

In this section, we have seen that variations in beam current affect both the relative efficiency and the five wire efficiency of the Region 3 VDCs. Both measures of efficiency decrease with increasing beam current. This trend can be explained by distruptions in the equilibrium state of the chamber. When the chambers are idle (i.e. no beam current), a characteristic electric field is set up between the high voltage planes and the wires. As a particle passes through a chamber and ionizes argon molecules, this characteristic field is upset. Positive ions drift towards the high voltage plane, while negative electrons drift towards the wires, thereby reducing the magnitude of this electric field. For small enough beam currents, the chambers will restabilize between electron tracks. However, increasing the beam current increases the

likelyhood that a second electron will pass through a region of the chamber, before the chamber has restablized from the first electron. In that case, the electric field may not be strong enough to induce an avalanche effect, and this second scattered electron may not be detected. Therefore, both the relative efficiency and the five wire efficiency decrease due to this effect.

We also saw that these beam current variations have little to no effect on the mean average residual of fitted tracks. In particular, no effect was observed on the mean average residual for multi-plane tree lines. There did appear to be a small correlation between single-plane tree line mean average residual and beam current. Based on the discussion above, we would not expect the residuals to increase with increasing beam current. An increase in beam current affects the efficiency due to disruptions in the electric field. However, once the characteristic electric field is restored, the chambers should be ready to detect electrons with the same level of resolution. The increase in average residual for single-plane tree lines is likely due to secondary particles. Increasing the beam current may increase the number of noise particles passing through the chambers. However, due to the trajectories of these particles, it is unlikely that they would produce multi-plane tree line events. Therefore, only the single-plane tree line residuals are affected by these noise particles.

4.4 Future Work

The research presented in the above sections uses the data currently available to provide an overview of chamber performance variations with running

conditions. Using these data, we were able to describe how chamber performance varies with VDC high voltage, VDC threshold voltage, and beam current. However, for the high voltage and threshold voltage studies, the data available do not allow for a complete, in-depth analysis of chamber behavior. For the high voltage studies, we studied how the applied high voltage affects chamber performance, at a threshold of 8 V. For a complete analysis, we would perform the same high voltage studies at multiple threshold values. Likewise, our threshold voltage studies look at variations in chamber performance with threshold voltage, at a high voltage of 3800 V. Further research would perform these threshold studies at multiple high voltage values. The values 8 V and 3800 V were used because preliminary analysis of chamber behavior suggested that these values produced a sufficient level of chamber performance. However, this preliminary analysis was not carried out using beam data from the experimental hall. We have already seen evidence that higher threshold voltages produce higher chamber efficiencies, and future data may indicate that other combinations of high voltage and threshold better optimize chamber performance. The level of future research into these questions will depend on the amount of beam time available to perform these additional high voltage and threshold studies.

Chapter 5

Conclusion

The research presented in this paper was focused on understanding how the Region 3 VDC performance varies with operating conditions. Chamber performance was studied with respect to high voltage, threshold voltage, and beam current. The purpose of the high voltage and threshold voltage studies was to find the optimal running conditions for the VDCs. The data included and the analysis that followed suggests that chamber performance is optimized for high voltages near 3800 V. For voltages below 3700 V, it was clear that the chambers were not operating at maximum efficiency. Above 3800 V, there was some evidence that tree line residual may increase, thereby decreasing track resolution. For threshold voltage, all data suggests that chamber performance is optimized for high thresholds. Increasing threshold voltage correlates with increasing efficiency and decreasing mean average residuals. Further research may be necessary to determine what upper limit should be imposed on the threshold voltage. The purpose of the beam current studies was to ensure that chamber performance is not heavily impacted by varia-

tions in the tracking mode current. Data for these studies was taken with beam currents significantly greater than those used for Q^2 measurements. It was observed that chamber performance decreases with increasing beam current. However, these variations in chamber performance are not expected to be of any significance at the lower current rates. Further research will look at how variations in these (and other) running conditions directly affect the measurements of Q^2. Accurate measurements of Q^2 are vital to Q_{weak}'s goal of making a precise measurement of the proton's weak charge.

Chapter 6

Bibliography

[1] Humensky, T.B. Ph.D. Dissertation: Probing the Standard Model and Nucleon Structure via Parity-Violating Electron Scattering. 2003.

[2] Griffiths, D. Introduction to Elementary Particles, 2nd ed. (Wiley-Vch, Weinheim, 2008).

[3] Perkins, D.H. Introduction to High Energy Physics, 2nd ed. (Addison-Wesley Publishing Company, Reading, 1982).

[4] Lee, T.D. and Yang, C.N. *Phys. Rev.* **104**, 254 (1956).

[5] Wu, C.S. et al. *Phys. Rev.* **105**, 1413 (1957).

[6] Armstrong et al. The Q_{weak} Experiment: "A Search for New Physics at the TeV Scale via a Measurement of the Protons Weak Charge." http://www.jlab.org/qweak/ , (Unpublished, Proposal Update to Jefferson Lab Program Advisory Committee) 2007.

[7] Bennett, S.C. and Wieman, C.E. *Phys. Rev. Lett.* **82**, 2484 (1999).

[8] Anthony, S.C. et al. *Phys. Rev. Lett.* **95**, (2005).

[9] Zeller, G.P. et al. *Phys. Rev. Lett.* **88**, (2002).

[10] Yao, W.M. et al. *J. Phys.* **G33**, (2006).

[11] Mitchell, J. http://hallaweb.jlab.org/document/OPMAN/node134.html. (Accessed 14 April 2011).

[12] Rachek, I. et al. New Amplifier-Discriminator Cards for Multiwire Drift Chambers. http://hallaweb.jlab.org.

[13] Zielinski, R.B. W&M Senior Thesis Project: Testing and Analysis of Q-Weak's Multiplexing Electronics System. 2010. (Unpublished)

[14] ROOT. http://root.cern.ch/drupal/.